Supplementary material: Seasonal input and flux error results

We have used annual summary plots in the main text to summarize the various OSSE inputs and assimilation results. While this saves space, it masks the strong variations in both the input and output across the seasonal cycle. Here we give several 32-panel summary plots with this seasonal detail.

The single-sounding measurement uncertainty patterns in Fig. S1a shift with the seasons as the SZAs shift north/south (Fig. 4a) and the median aerosol ODs (Fig. S1e) change with the seasons, particularly around the Sahara, the Middle East, central and east Asia, and certain ocean areas. The lowest single-sounding measurement errors are found over the high latitude oceans during the winter solstice in glint mode, where the high SZAs give the lowest ocean errors. However, the glint mode path length correction for clouds at these high SZAs (compare the pre- and post-correction glint mode cloud amounts in Fig. S2h and S2f) more than cancels out these lower errors: the number of effective measurements per 1x1 area (Fig. S2b) drops to its lowest values then due to difficulty finding cloud-free soundings, and the resulting glint mode multi-sounding measurement errors (Fig. S1d) are higher then than in the local summer. A SZA-dependent trend in the single-sounding measurement errors in the opposite direction occurs over the high-latitude northern land areas (lower measurement errors in the local summer), but because cloud effects do not dominate there, the multi-sounding measurement errors remain lower in the local summer, in phase with the errors over the ocean. The lowest measurement errors in both nadir and glint mode are achieved over dry areas that have low cloud amount while at the same time are not covered by thick aerosol layers: Australia, South Africa, and the northern Sahara, all in the local spring/summer.

These seasonal changes in the effective multi-sounding measurement uncertainties are convoluted with seasonal changes in the location of predominantly rising and subsiding air over the extratropical land and ocean areas to give the seasonal shifts in the 7-day flux error reductions in Fig. S5. In glint mode over the oceans, the largest reductions occur when the sun is

highest overhead, mainly due to the SZA-dependent reduction in cloud-free availability we use here giving lower effective measurement uncertainties. Figure S4 gives the seasonally-varying flux errors from which the error reductions are computed. Because of the strong variability in the prior-truth flux differences (with the greatest differences over the extratropical vegetated land areas during the growing season), there is also strong variability in the a posteriori flux errors: they are higher when the a priori errors are also higher, in keeping with the fractional error reductions being more constant. The seasonal mean flux errors given in Fig. S3 seem to show an opposite behavior, at least in the perfect model experiments, with the lowest errors occuring during the northern growing season and the largest biases occuring in the far north during local winter.

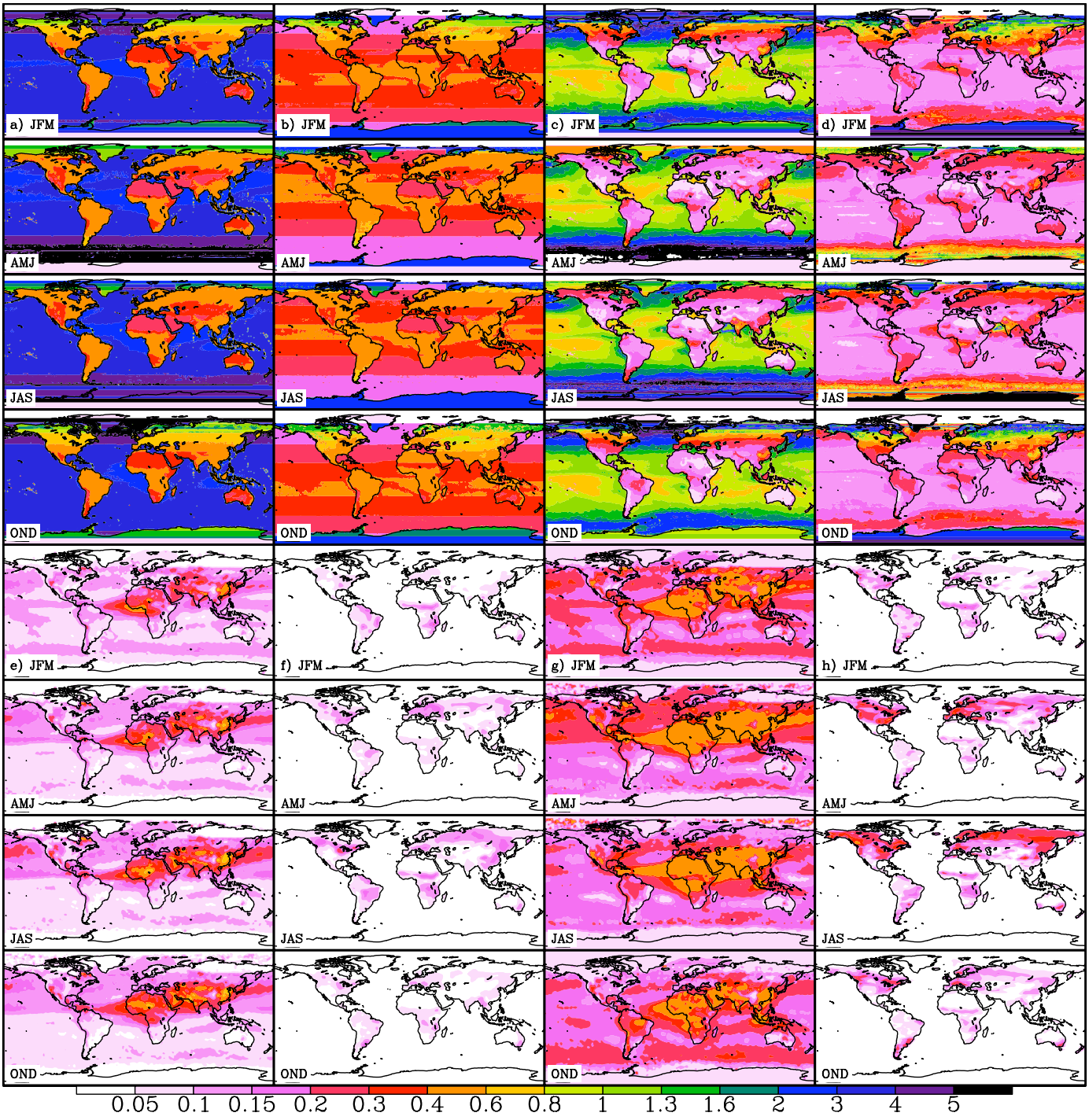

Figure S1: Seasonal results (Jan-Mar, Apr-Jun, Jul-Sep, Oct-Dec) for: the single-sounding OCO X_{CO2} retrieval uncertainties σ_{1_shot} computed in Bösch, et al. for a) nadir and b) glint viewing modes; the effective multi-sounding OCO X_{CO2} measurement uncertainty σ_{eff} for all valid retrievals inside each 1º latitude band along a single sun-lit pass of the OCO orbit, computed as $\sigma_{eff} = \sigma_{1\_shot}/\sqrt{N_{eff}}$, for c) nadir and d) glint modes; e) the median aerosol OD at 760 nm, computed from Aqua/MODIS data according to the procedure outlined in Bösch, et al; f) the assumed spatial representation error, extrapolated from the two sites in Corbin, et al (2008) using a pattern proportional to the a priori net flux magnitudes; g) the uncertainty added in quadrature to the assumed measurement uncertainties to account for the impact of aerosol biases in Experiments 4 & 6 (twice this is added in #4b & 6b); and h) the uncertainty added to the assumed measurement uncertainties to account for the impact of transport errors in Experiments 3, 6, and 6b.

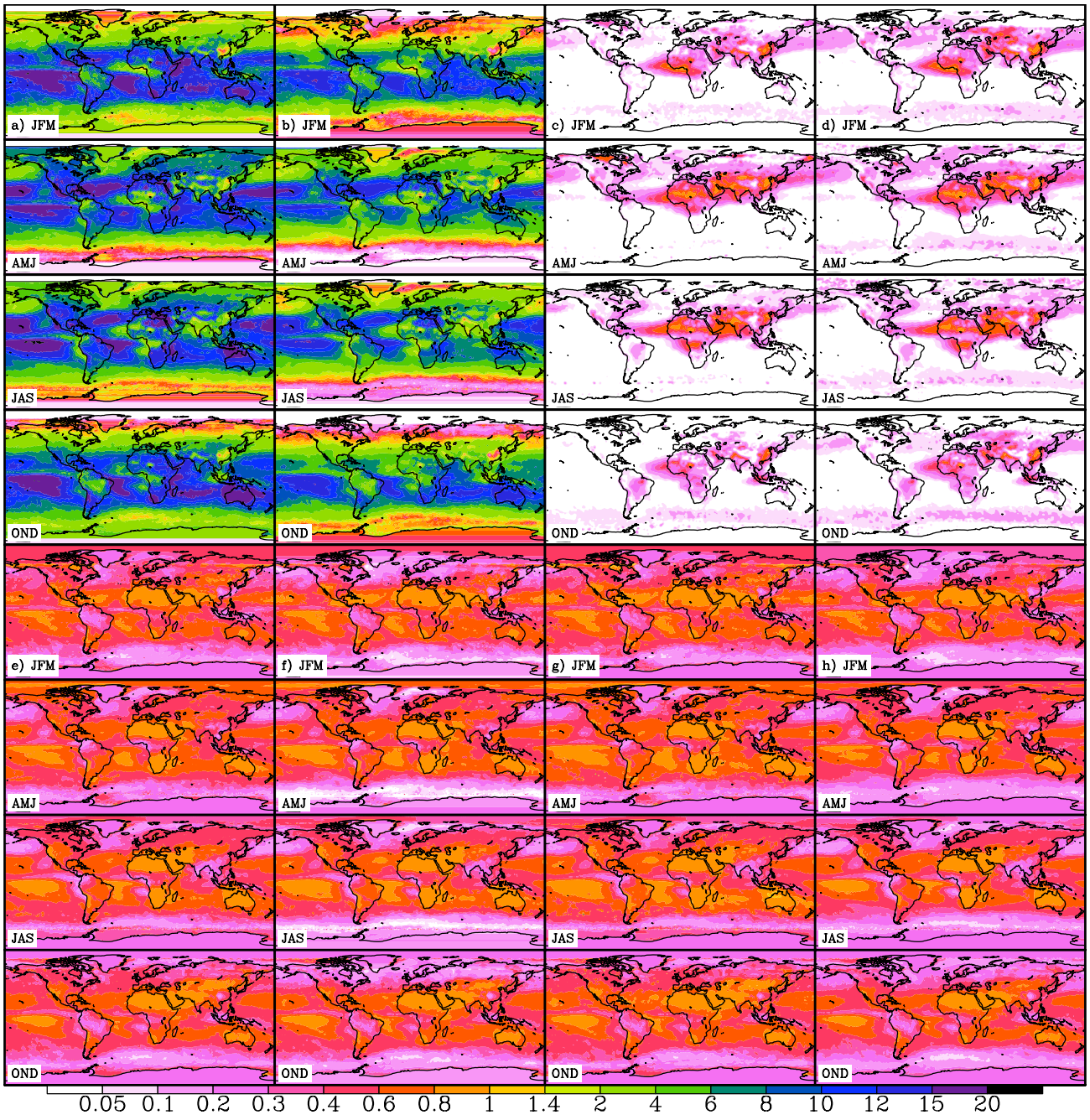

Figure S2: Seasonal results (Jan-Mar, Apr-Jun, Jul-Sep, Oct-Dec) for: the effective number of independent X_{CO2} measurements N_{eff} in each 1º latitude band for a single sun-lit pass of the OCO orbit for a) nadir and b) glint viewing modes; the pathlength-corrected probability P_{HiAeroOD} of encountering aerosol ODs at 760 nm of greater than 0.30 computed from Aqua/MODIS data for c) nadir and d) glint viewing modes; the path-corrected probability $P_{\text{cloud-free}}$ of finding at least one cloud-free X_{CO2} measurement inside a portion of the OCO FOV ground track of length L (Fig. 5b), calculated from MODIS data according to the procedure outlined in the Appendix, for e) nadir and f) glint modes; g) the cloud-free probability at 1km x 1km resolution, taken from the Aqua/MODIS Level 3 data cloud-mask product; and h) the probability $P_{\text{cloud-free}}$ of finding at least one cloud-free X_{CO2} measurement inside a portion of the OCO FOV ground track of length L *before* path correction. Note that the cloud correlation length L is longer in glint mode than nadir, resulting in higher $P_{\text{cloud-free}}$ values; however, since a longer L also results in fewer potential independent soundings per grid box, the glint mode N_{eff} ends up being lower than in nadir mode.

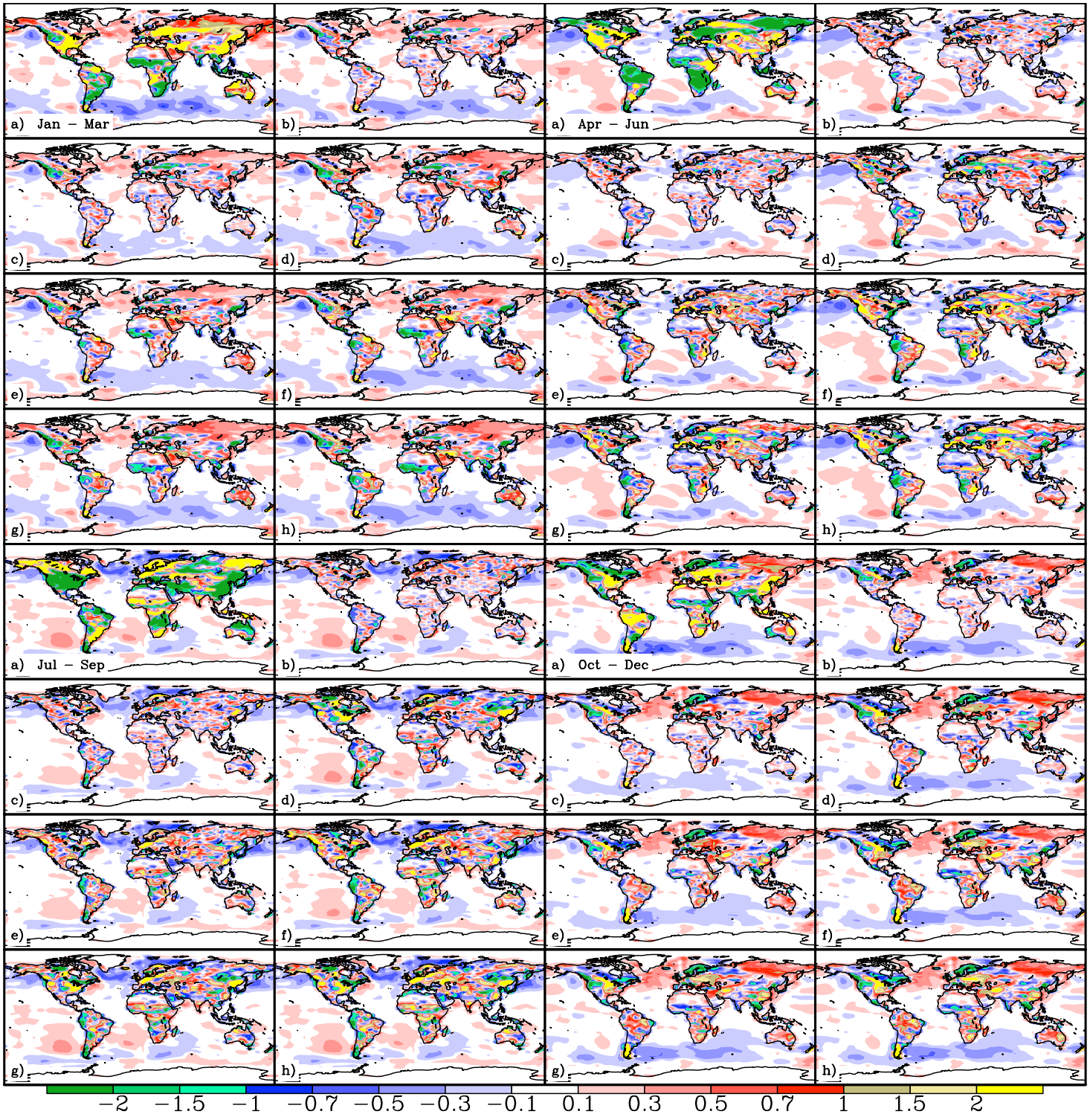

Figure S3: Seasonal mean flux errors [10^{-8} kgCO2 m^{-2} s^{-1}] for Jan.-March (upper left), April-June (upper right), July-Sept. (lower left), and Oct.-Dec. (lower right) using glint mode data after 50 iterations for the following experiments: c) #2, d) #5, e) #4, f) #4b, g) #6, and h) #6b. Also given: a) the a priori flux differences and b) seasonal mean flux errors given using nadir mode data after 50 iterations.

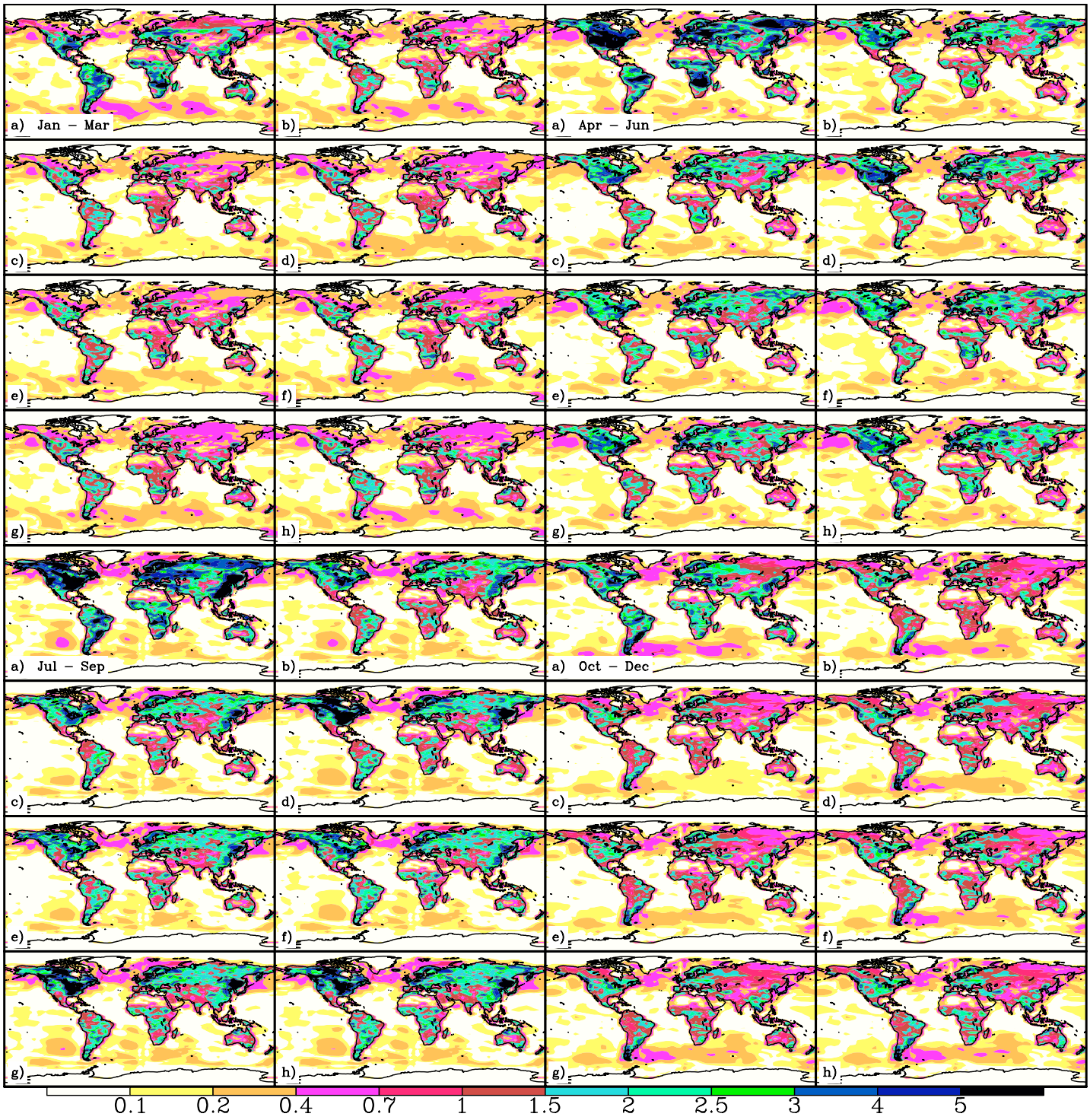

Figure S4: RMS 7-day a posteriori CO_2 flux errors [10^{-8} kg CO_2 m^{-2} s^{-1}] for Jan.-March (upper left), April-June (upper right), July-Sept. (lower left), and Oct.-Dec. (lower right) using glint mode data after 50 iterations for the following experiments: c) #2, d) #5, e) #4, f) #4b, g) #6, and h) #6b. Also given: a) the a priori flux differences and b) the RMS 7-day flux errors given using nadir mode data after 50 iterations.

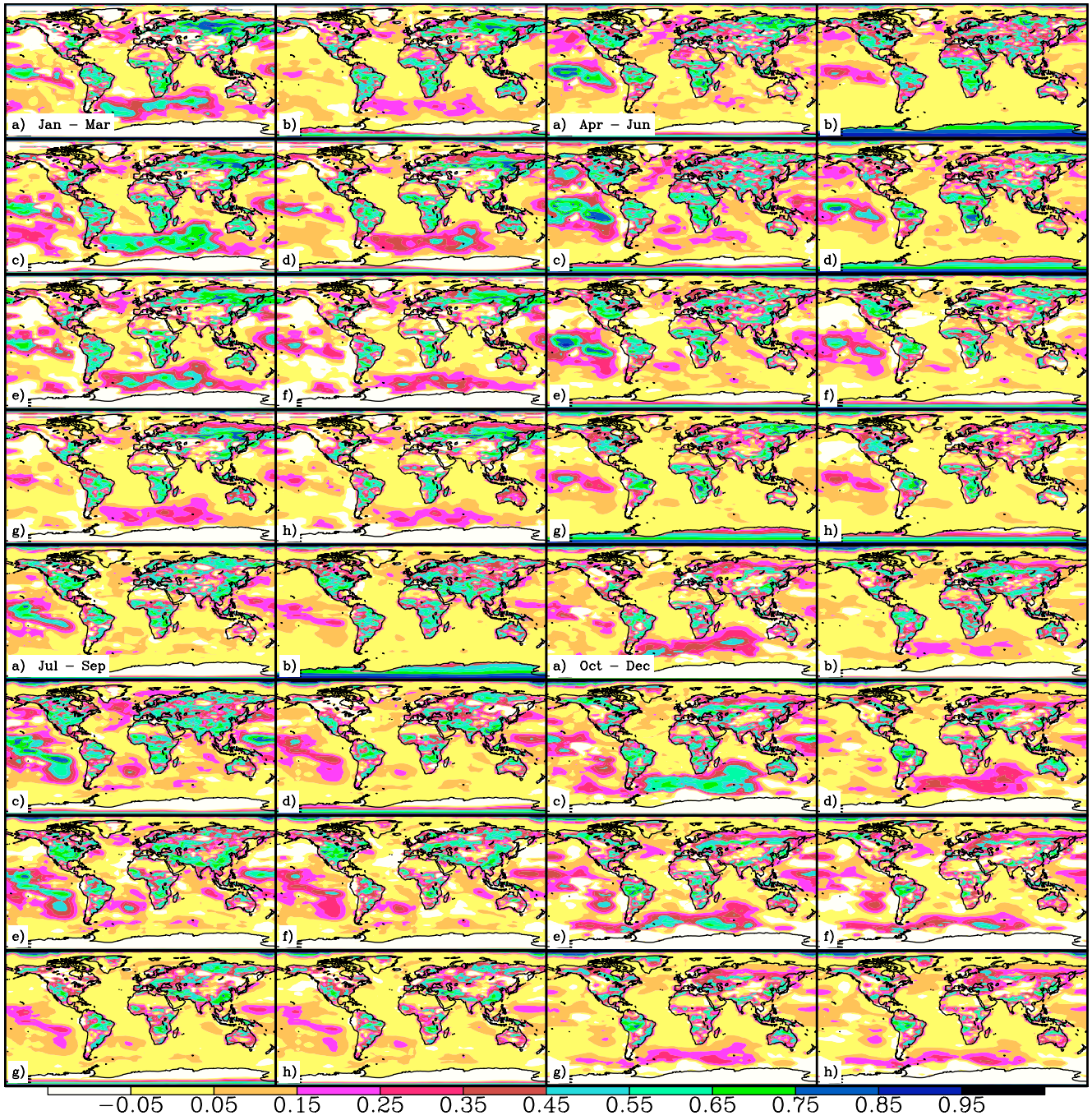

Figure S5: Fractional error reductions in 7-day CO_2 fluxes, computed across Jan.-March (upper left), April-June (upper right), July-Sept. (lower left), and Oct.-Dec. (lower right) from the RMS flux differences in Fig. S4 obtained using glint mode data after 50 iterations for the following experiments: c) #2, d) #5, e) #4, f) #4b, g) #6, and h) #6b. Also given are the fractional error reductions obtained using a) glint mode data after 130 iterations of the mistuning experiment (#3), and b) nadir mode data after 50 iterations (Experiment #1).